Fuzzy Logic based Multi-Dimensional Image Fusion for Gas-Oil-Water Flows with Dual-Modality Electrical Tomography

Qiang Wang, Xiaodong Jia, and Mi Wang

Abstract—This paper proposes a novel approach whereby fuzzy logic and decision tree are utilised to overcome the challenges in analysing images of gas-oil-water pipeline flow obtained using electrical resistance and capacitance dual-modality tomography. The approach firstly generates two axially-stacked concentration images from two stacks of the cross-sectional concentration tomograms reconstructed from different modalities respectively, and then registers two generated images in temporal and spatial terms. Afterwards, a fuzzy logic method is applied to perform a pixel-level fusion to integrate the registered images based on the characteristics of electrical tomograms for multi-phase pipeline flow. Later, a decision tree is utilised to derive the local concentration of each individual phase according to the fusion results. Using the data from real industrial cases, both feasibility and robustness of the proposed approach are demonstrated. In addition, the proposed approach also overcomes the limitations of conventional threshold-based methods on the request of *priori* knowledge for the qualitative and quantitative analyses of gas-oil-water pipeline flow.

Index Terms—Multi-dimensional data fusion, dual-modality electrical tomography, fuzzy logic, decision tree, gas-oil-water flow, multiphase flow visualisation.

I. INTRODUCTION

The world consumes a great amount of energy every year, and over 60 % of which is from oil and gas. In 2016, over 4400 million metric tons of oil and 27 trillion cubic feet of natural gas have been consumed, contributing tremendously to the world economic value [1]. When oil is extracted from a well, it usually exists as a multiphase flow, containing time-varying ratios of oil, water, and gas. Due to the unpredictable and complicated presentations of individual phases and opaque nature of crude oil, it is extremely challenging to quantify and qualify such flows. At present, the uncertainty is typically up to 20% [2]. Therefore, ability to quantify and qualify such flows more accurately has ongoing financial implications.

Process tomography as a non-intrusive/invasive approach has been intensively investigated and applied to multiphase flow visualisation and measurement [3]. In general, it utilises the difference of a physical property to distinguish different phases. For example, electrical resistance tomography (ERT) differentiates gas from water by electrical conductivity and electrical capacitance tomography (ECT) differentiate water from oil and gas by electric permittivity difference. However,

Q. Wang's current contact is with School of Chemistry, University of Edinburgh, Edinburgh EH9 3JF, UK (email: q.wang@ed.ac.uk).

Q Wang, X. Jia, and M. Wang are with the School of Chemical and Process Engineering, University of Leeds, Leeds LS2 9JT, UK (email: x.jia@leeds.ac.uk; m.wang@leeds.ac.uk).

single-modality electrical tomography is unable to measure and/or visualise three-phase flow, e.g. gas-oil-water flow, which is a common factor in oil and gas production. Therefore, additional modality, in the form of dual-modality tomographic systems (DMTS), could overcome the challenges in three-phase flow [4].

Dual-modality tomographic systems, i.e. simultaneously employing two different tomographic systems to tackle the three-phase phenomenon, have been applied to many areas, such as those applied in medical imaging and process engineering [4], [5]. The primary purpose of these applications is to overcome the limitations of single tomography by integrating complementary information from both tomography [5]–[7]. As far as the measurement and visualisation of gas-oil-water flow by DMTS are concerned, the research is still at its early stage, and the majority of the attention has been paid to the hardware, e.g. integrating different sensors together [8]–[10]. Among exsiting DMTS, ERT-ECT systems are a particular example characterised by low-cost, non-intrusive/invasive and non-radioactive electrical tomography. Electrical tomograms are usually high in temporal resolution but relatively low in spatial resolution [11], [12]. Some efforts have been made to exploit dual-modality ERT-ECT systems for multiphase flow imaging, such as gas-liquid flow or gas-oil-water three-phase flow, but the majority dealt with the hardware integration rather than systematic study of data fusion [13]–[16].

Image fusion in DMTS for multiphase flow visualisation and measurement could be applied before, during, or after image reconstruction. In practice, however, the pre-reconstruction fusion performed on raw signal data so far does not exist [17]. The reconstruction-level fusion refers the data fusion process during the image reconstruction. One set of data obtained with one tomographic system provides complementary information for the reconstruction process of the other tomographic system, where no further processing is required after the reconstruction of the second system. To our best knowledge, such fusion technique is not available to date either. Therefore, all existing image fusion approaches for DMTS-based multi-phase flow characterisation are performed on the individually-reconstructed data by the involved modalities, i.e. the image-level fusion.

As far as pixel-level image fusion is concerned, many fusion algorithms have been proposed for tomography-based applications, e.g. wavelet transform and fuzzy logic in medical imaging [5]. At the first glance, it may seem trivial to directly apply those fusion algorithms to multiphase flow visualisa-

tion. In reality, it introduces several technical challenges. For example, the spatial-resolution of electrical tomograms is too low to distinguish small bubbles below a certain size, and there are no sharp boundaries between the dispersed phase and continuous phase. Comparing the modalities of ultrasound or x-ray imaging with electrical tomography, the significant difference is that electrical tomography is a 'soft field' tomographic technique, whereas the techniques for medical imaging are usually based on 'hard field' [3]. Images produced with hard field tomography systems normally have a spatial resolution higher than that by electrical tomographic systems. For example, advanced X-ray computed process tomography is capable of detecting small particles at 1 mm level within a 60 mm bubble column, and thus generating high-quality reconstructed images [18]. In contrast, electrical tomography normally has a spatial resolution of 5%, i.e. the ratio of the largest detectable object to the size of the container [11]. This situation becomes worse when single-step linear back-projection (LBP) image reconstruction algorithm is used for reconstruction. In addition to the limitations by the modalities, the nature of multiphase flow also introduces extra challenges, such as flow dynamics, which demands the involved fusion has to take account of temporal information.

Another prominent challenge for data fusion in DMTS is that the resultant tomograms are not only informative about flow dynamics, e.g. flow regimes, but also quantitative in revealing time-varying ratio of individual phases, which is usually secondary in other fields. From this perspective, the conventional evaluation criteria, e.g. mean squared error (MSE), in other data fusion methods may be insufficient. Instead, the difference between the mean concentration from fused results and reference concentration is the primary criterion. Therefore, there are two types of references conventionally used for evaluating data fusion in DMTS: one is reference images, such as images taken with high-speed video logger, and the other is the mean concentration reference.

Using thresholds to determine geometrical distributions of gas-oil-water flow is the predominant method for DMTS to visualise gas-oil-water flow [10], [13], [17], [19]. In the threshold method, the original images are binarised by different threshold values which are usually modality specific. Later, the binarised images are fused. Thresholding is comparatively easy to be perceived and implemented, and requires limited computational resources. The values, however, have significant impact on the determination of phase concentration, of which a small deviation may result in considerable errors. Moreover, the pinpointing of the values is theoretically and practically challenging, since they may be influenced by many factors, such as the hardware, phase properties of the flow under investigation, and so on.

A few of advanced algorithms have been proposed without threshold values. Yue *et al.* [20] utilised fuzzy clustering algorithms to fuse the data from different sensing strategies, as well as ERT and ECT, for two-phase flow. Their results yielded comparable phase concentration with those observed references. However, whether their approach is applicable to three-phase flow remains a question since there is a fundamental difference between two-phase flow and three-phase due to

the introduction of an extra phase. Pusppanathan *et al.* [21] proposed fuzzy logic for ultrasonic tomography (UT) and ECT to integrate separately reconstructed images. The proposed method, however, was still at the stage of proof of concept and only evaluated at spatial dimension with simulated data. The authors have compared the performance of the proposed approach in this study with the conventional threshold-based method at 9th World Congress on Industrial Process Tomography [22], and this report is to comprehensively describe the approach used for the comparison.

This paper aims to overcome the challenges in qualification and quantification of gas-oil-water horizontal flow with dual-modality electrical tomography, with the assistance of fuzzy logic and decision tree. In this study, it is assumed that the flows investigated are fully developed in horizontal pipeline, and therefore it is reasonable to further assume that the tomograms from ERT and ECT are symmetrical to the vertical diameter, thereby the whole tomograms being approximated by one column averaged with a few columns at central area of the tomograms. In contrast to the existing arts, this study utilises fuzzy logic to integrate the concentration tomograms from ERT and ECT, and applies decision tree to decompose individual phases so that local phase void fraction can be derived. In addition, this study evaluates the feasibility and robustness of the proposed approach with the data from an industrial-scale three-phase flow testing facility, which covers commonly-observed flow regimes, i.e. (wavy) stratified flow, slug flow, plug flow, annular flow, and bubbly flow.

The rest of paper is arranged as follows. Section II briefly introduces the ERT-ECT systems applied in this study. The details of the approach are explained in Section III, and evaluation of the approach is presented in Section IV. Conclusion is made in Section V.

II. ELECTRICAL TOMOGRAPHY

Electrical tomography is a set of techniques that utilises electromagnetic principles to sense the electrical property distribution within the interested domain. The differences between electrical tomography methods are generally defined by targeted electric/dielectric properties of materials and associated sensor electronics, for example, the conductivity or permittivity and the associated excitation frequency and electrode size, in respecting to electrical resistance tomography or electrical capacitance tomography. Electrical impedance tomography (EIT) is a general definition for a method that can measure electrical impedance of materials by targeting both conductivity and permittivity properties of mixture. Both ERT and EIT utilise the variation of conduction current but ECT utilises the variation of displacement current to detect the process variation.

Due to the nature of the electrical field, electrical tomography is incapable of having homogeneous sensitivity distribution over its sensing domain [23], which results in the inhomogeneity of sensing outcome, e.g. the same object at different positions within the sensing area of electrical tomography may produce differences in their tomograms. In addition, ill-conditioned problems in association with inverse solution
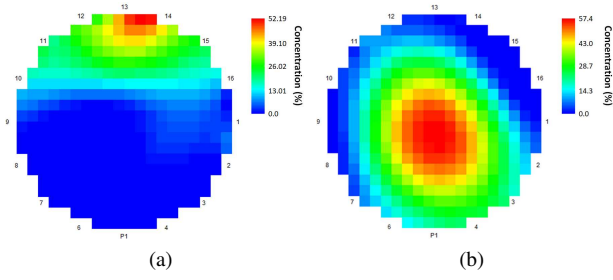
Fig. 1. ERT-based concentration tomograms of a bubbly flow (a) and a slug flow (b) in a horizontal pipe, reconstructed with LBP.

and limited number of measurement also cause problems for electrical tomography. A direct consequence of the limitations is that the tomograms are unable to indicate small bubbles below a certain size. In addition, it cannot provide sharp interfaces between large bubbles and the liquid phase. Fig. 1 depicts the incapability of ERT tomograms, in which small bubbles in a bubbly flow disappear (Fig. 1a). In Fig. 1b, the tomograms show only the rough existence of a large bubble in a slug flow, but the boundary is too blurred to be identified. Nonetheless, electrical tomography is still able to handle gas-liquid flow with up to 100% gas concentration [24].

After ERT/ECT tomograms are reconstructed, the Maxwell-Garnett formula [25] can be applied to derive local void fraction of interests. In the case of gas-oil-water flow, the local void fraction in an ERT tomogram represents the fraction of the non-conductive phase, i.e. gas and oil, whereas the corresponding one in an ECT tomogram reveals the proportion of the gas phase. Together with the conservation law, i.e. the sum of phase concentrations at any pixel is 100%, the local concentration of each phase can be determined by solving three linear equations with three unknowns:

$$C_{water} + C_{oil} + C_{gas} = 100\% \tag{1}$$
$$C_{oil} + C_{gas} = M_{ERT} \tag{2}$$
$$C_{gas} = M_{ECT} \tag{3}$$

where C_x is the local concentration of each phase, and M_x is the measured concentration of ERT or ECT. It is worthwhile to mention that (2) is derived based on the assumption that gas and oil conductivity is zero, and (3) is obtained also by applying Maxwell relationship with the assumption that the difference of permittivity oil and water is ignorable due to their large difference from the permittivity of gas.It seems the linear equation group ((1) to (3)) with disperse phase concentrations derived from ERT and ECT should result in a complimentary and unique solution for three-phase phase concentration in a pixel. However, the inherent limitations of ERT/ECT may provide significant error, e.g. under-determination or over-determination of phase concentrations to dissatisfy the (1).

In this study, standalone ERT and ECT systems are deployed to obtain conductivity and permittivity distribution on gas-oil-water horizontal flow. Reconstructed tomograms from ERT are arranged in 20×20 grid, whereas ECT tomograms are with 32×32 grid. During the operation, the data acquisition speed (DAS) of ERT and ECT is set to 62.5 fps and 12.5

fps, respectively. Afterwards, the reconstructed tomograms are converted to concentration distribution of the relevant phases. The converted concentration tomograms are eventually used as the input to the proposed fusion approach. It is worth pointing out that in this paper, the terms *data*, *tomogram*, and *image* are used interchangeably for cross-sectional tomographic images.

III. METHODOLOGY

Since concentration tomograms from ERT and ECT are acquired with different spatial and temporal resolutions, and represent different phases, they have to be pre-processed before entering into the fuzzy inference system (FIS). After pre-processing, the data (over the axial cross-section of pipeline) are translated into linguistic values according to their pixel values, as the input for FIS. The linguistic values are inferred to a single value using pre-defined membership functions and fuzzy rules, of which the value implies possible combination of each phase. By using a decision tree, the mixture at each pixel is decomposed into phases and their local concentrations, and the results are finally displayed using conventional colour mapping. The schematic diagram of the processing is depicted as Fig. 2, and each step is discussed in the following sections.

A. Image pre-processing

The major objective of this step is to generate registered stacked tomograms from the input cross-sectional concentration tomograms. The procedure of this step is demonstrated in Fig. 3. The input images at this stage are two stacks of cross-sectional concentration tomograms by ECT and ERT using ITS Toolsuite software [26]. Let $C^E = \{c_i^E \mid i \in \{1, 2, \cdots, N^E\}\}$ denote a cross-sectional image with N^E number of pixels by ECT or ERT, where E is either ERT or ECT. Consequently, the input images can be symbolised as:

$$\mathbf{I}^E = \{C^{E_i} \mid i \in \{1, 2, \cdots M^E\}\} \tag{4}$$

where i represents ith image in M^E for E. In order to reflect temporal information relating to flow regimes, axial cross-sectional images are also generated by stacking a number of consecutive tomogram segments extracted from central vertical area of the original tomograms. In order to diminish the error caused by the approximation of the whole tomograms with a central column, the data of 4 central columns is averaged. Stacked images $\mathbf{SI}^E$ for ERT and ECT can be defined by (5) and (6), respectively:

$$
\begin{aligned}
\mathbf{SI}^{ERT} &= \{si_j^{ERT_i} \mid si_j^{ERT_i} = \\
&\frac{1}{2}(c_{119+j}^{ERT_i} + c_{139+j}^{ERT_i} + c_{159+j}^{ERT_i} + c_{179+j}^{ERT_i}), \\
&i \in \{1, 2, \cdots, M^{ERT}\}, j \in \{1, \cdots, 20\}\}
\end{aligned} \tag{5}
$$

$$
\begin{aligned}
\mathbf{SI}^{ECT} &= \{si_j^{ECT_i} \mid si_j^{ECT_i} = \\
&\{\frac{1}{2}(c_{451+j}^{ECT_i} + c_{481+j}^{ECT_i} + c_{511+j}^{ECT_i} + c_{541+j}^{ECT_i}), \\
&i \in \{1, 2, \cdots, M^{ECT}\}, j \in \{1, \cdots, 32\}\}
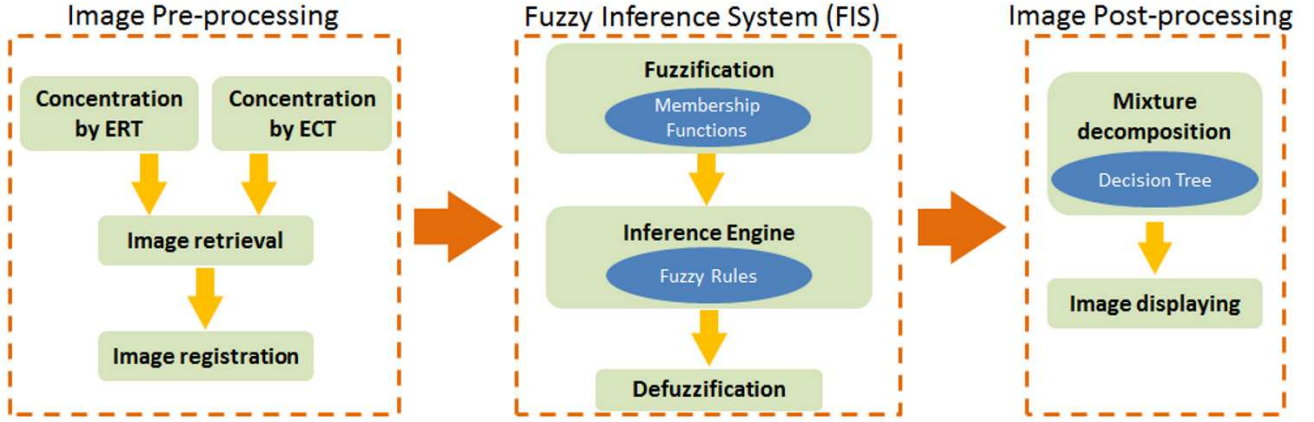\end{aligned} \tag{6}
$$

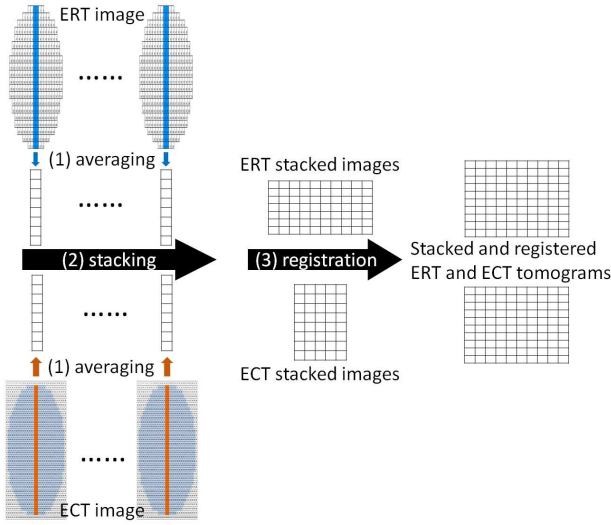Fig. 2. Schematic diagram of the proposed approach.

Fig. 3. The procedure of image pre-processing at pixel level: (1) averaging four central columns in the original ERT and ECT tomograms respectively to one column; (2) stacking all averaged columns in sequence for ERT and ECT respectively; (2) registering the stacked ERT and ECT images in spatial and temporal terms.
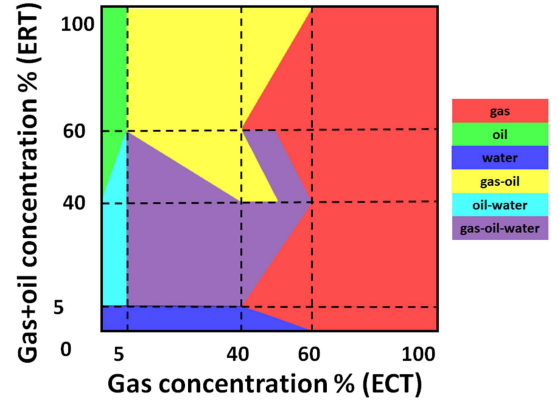

Fig. 4. Possible phase combinations based on the disperse phase concentration distributions, i.e. gas+oil and gas by ERT and ECT, respectively.

where the numbers *119*, *139*, *159* and *179*, and *451*, *481*, *511*, and *541* are the pixel indices in the ERT and ECT images, respectively.

Since ERT and ECT work at different frequency and produce different sizes of tomograms, resulting in the concentration tomograms with different spatial and temporal resolution, the generated axial stacked images have to be transformed to a common coordinate system before image fusion. A general transform function can be defined as:

$$(\mathbf{S}', t') = T(\mathbf{S}, t) = (T_{\mathbf{S}}(\mathbf{S}, t), T_t(\mathbf{S}, t)) \tag{7}$$

where $(\mathbf{S}', t')$ is the target coordinate system, including space and time, $(\mathbf{S}, t)$ is the original coordinate system, and $T_{\mathbf{S}}(\mathbf{S}, t)$ and $T_t(\mathbf{S}, t)$ are spatial and temporal transformation functions of $\mathbf{S}$ and t. However, in practice, the (7) is approximated by decoupling the equation to

$$(\mathbf{S}', t') = (T_{\mathbf{S}}(\mathbf{S}, t), T_t(\mathbf{S}, t)) \approx (T_{\mathbf{S}}(\mathbf{S}), T_t(t)) \tag{8}$$

According to Fig. 3, $\mathbf{SI}^E$ already reflects space and time. Therefore, $(\mathbf{S}', t')$ can be simplified to $(\mathbf{SI}^E)'$. Then, applying (5) and (6) to (8), we have:

$$(\mathbf{SI}^E)' = (T_{SI}^E(\mathbf{SI}^E), T_t^E(\mathbf{SI}^E)) \tag{9}$$

Transform functions $T_{\mathbf{SI}}^E$ and T_t^E could be any functions which are able to generate the transformation results at the same spatial and temporal positions. In our case, linear interpolation is employed for all transform functions due to its computational and implementational simplicity. Finally, the original two stacks of cross-sectional ERT and ECT tomograms are processed to reflect the compatible informative content in spatial and temporal terms.

B. Fuzzy Inference System

It is well known that the derived concentration tomograms by electrical tomography have a close relationship with the phases in gas-oil-water flow. As far as ERT is concerned, the concentration range [0%, 100%] can be split into four sections: the low-, low-mid-, mid-high-, and high-concentration section. In the low-concentration section, flow is assumed to be only water due to noise, and 5% is chosen as the

boundary value [11]. In the low-mid-concentration section, it is believed that flow is a mixture of the conductive phase (water) and the non-conductive phase (gas and oil). In the high-concentration section, it is believed that flow contains only the non-conductive phase, i.e. gas and oil. In the mid-high-concentration section, flow components can be either a mixture of the conductive and non-conductive phases or purely the non-conductive phase. The boundary values are defined as 40% and 60% for demonstration purpose.

Similar principle can be applied to ECT as well. In the low-concentration section, flow is assumed to contain only the oil and water phase. In the low-mid-concentration section, flow contains a mixture of gas, oil, and water. In the high-concentration section, flow contains only the gas phase. In the mid-high-concentration section, flow contains either a mixture of all components or only the gas phase.

Using ECT concentration as X axis and ERT concentration as Y axis, a map can be drawn to split the whole range to different sub-ranges. Each sub-range reflects the possible components in the flow under investigation for the given concentration values from ERT and ECT, depicted in Fig. 4. Some sub-ranges containing single colour reflect that flow has certain component(s), whereas others containing more than one colour indicate flow could have different combinations of the phases. The latter is due to the limitation of electrical tomography when visualising multiphase flow. Following this fundamental principle, a fuzzy inference system (FIS) can be constructed to determine possible combinations of the gas, oil, and water phases, as well as the probability of each combination if there are more than one combinations. With the combinations and the probability, mixture can be decomposed into individual phase and concentration values of each phase can be estimated. Overall, the FIS for our purpose has two inputs from ECT and ERT images and two outputs for *gas+oil* and *oil+water*. The inputs are fuzzified firstly using membership functions to obtain corresponding membership degrees. Afterwards, a number of fuzzy rules are all evaluated according to the membership degrees, of which the results are aggregated for later process. Finally, the aggregation is defuzzified to a crisp value as a basis for the decomposition and estimation.

1) Fuzzification: The purpose of fuzzification is to translate input fuzzy variables, i.e. mapping concentration values, to membership degrees at [0, 1]. Let a universe of discourse (UOD) $U = (\mathbf{SI}^E)'$, i.e. the registered images from pre-processing. Then, a fuzzy set F^E, based on the images can be defined [27].

$$F^E = \{(\mu_F(p^E)/p^E | p^E \in U)\} \quad (10)$$

where p^E is an element in the input images, and $\mu_F(p^E)$ is a fuzzy membership function (MF) of p^E in the set F^E which maps the p^E into the closed interval $[0,1]$, i.e. $\mu_F(p^E) : F^E \to [0,1]$. In this paper, triangle-shaped MF is chosen for *low-mid* and *mid-high* segments, due to it is easy to be implemented and insensitive to errors [28], whereas trapezoidal-shaped MF is utilised for *low* and *high* segments, because of the complete and full membership to

satisfy $\mu_F(p^E) = 1$. Triangle-shaped MF and trapezoidal-shaped MF are given by (11) and (12) respectively.

$$\mu_F(p^E) = \mu_F(p^E) = \begin{cases} 0 & p < a \\ \frac{p^E - a}{b - a} & a \leq p^E \leq b \\ \frac{c - p^E}{c - b} & b \leq p^E \leq c \\ 0 & p^E \geq c. \end{cases} \quad (11)$$

$$\mu_F(p^E) = \begin{cases} 0 & p < x \\ \frac{p^E - x}{y - x} & x \leq p^E \leq y \\ 1 & y \leq p^E \leq z \\ \frac{w - p^E}{w - z} & z \leq p^E \leq w \\ 0 & p^E \geq w. \end{cases} \quad (12)$$

The a and c are so-called *bases*, and b is so-called *peak* for triangle-shaped MF. Similarly, the x and w are so-called *bases*, and y and z are so-called *shoulders* for trapezoidal-shaped MF. Integrating the principle in Fig. 4 with (11) and (12), the MFs can be defined for the two fuzzy sets by ECT and ERT, as depicted in Fig. 5, and the values for a, b, c, x, y, z, and w are defined in Table I. It is worth pointing out that there are overlapped ranges between the sections because the actual boundary values splitting the concentration range are unable to be determined but are believed to be within the overlapped ranges.

2) Inference engine: Inference engine performs the implications from antecedent to consequence using pre-defined *if antecedent then consequence* rules and fuzzy logic operators. According to Fig. 4, the fuzzy rules are defined in Table II. A percentage is also calculated as the weight for each rule by the ratio of the area of each case to the whole area in the Fig. 4. When there are more than one possible combinations in a case, it assumes that the possibility for every combination is the same, thereby the percentage is evenly divided by the number. In addition, if the mixture includes *water+oil+gas*, the consequence is set with two parts: one is *gas+oil*, and the other is *oil+water*. That is, the implication engages both output MFs.

As far as fuzzy logic operators are concerned, the intersection (AND), union (OR), and complement (NOT) are defined using *min*, *max*, and *complement* as:

$$\mu_{F_{ERT} \cap F_{ECT}}(p) = min\{\mu_F(p^{ERT}), \mu_F(p^{ECT})\} \quad (13)$$

$$\mu_{F_{ERT} \cup F_{ECT}}(p) = max\{\mu_F(p^{ERT}), \mu_F(p^{ECT})\} \quad (14)$$

$$\mu_{\overline{F}}(p^E) = 1 - \mu_F(p^E) \quad (15)$$

With (13), (14), and (15), the antecedent in a rule is evaluated to obtain one number that represents the degree of that antecedent. The number is then applied to an output MF to infer a subset of the fuzzy set represented by the consequence. In our case, the output MF utilises triangle-shaped MF as well, including all possible phase combinations, illustrated in Fig. 6, and related a, b, and c are defined in Table III. After all rules
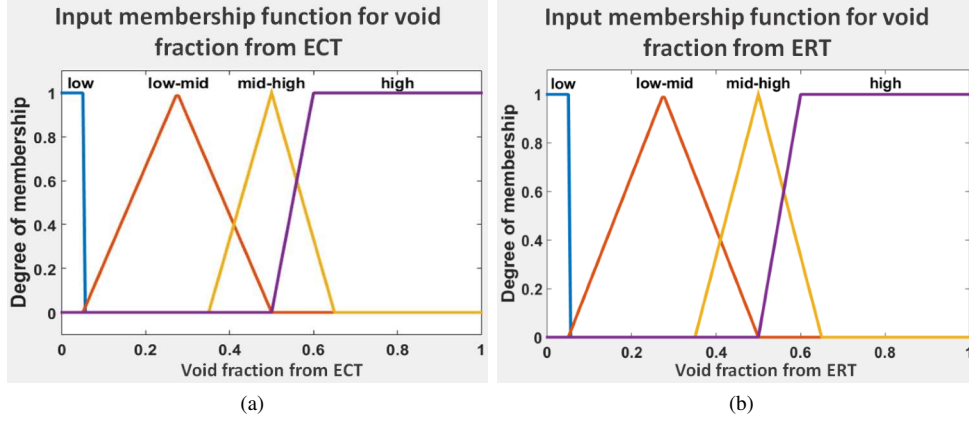
Fig. 5. The input membership functions for the void fraction from ECT (a) and ERT (b).

TABLE I
PARAMETERS FOR THE INPUT MEMBERSHIP FUNCTIONS BASED ON VOID FRACTION.

	ECT	ERT
low	-0.3 (x), -0.0333 (y), 0.05 (z), 0.05 (w)	-0.3 (x), -0.0333 (y), 0.05 (z), 0.05 (w)
low-mid	0.05 (a), 0.275 (b), 0.5 (c)	0.05 (a), 0.275 (b), 0.5 (c)
mid-high	0.35 (a), 0.5 (b), 0.65 (c)	0.35 (a), 0.5 (b), 0.65 (c)
high	0.5 (x), 0.6 (y), 1.033 (z), 1.3 (w)	0.5 (x), 0.6 (y), 1.033 (z), 1.3 (w)

TABLE II
FUZZY RULES WITH WEIGHTS FOR THE POSSIBLE COMBINATIONS OF THE WATER (W), OIL (O) AND GAS (G) PHASE.

$ECT \backslash ERT$	Low	Low-Mid	Mid-High	High
Low	W (0.25%)	W+O (1.25%)	W+O/O (0.5%)	O (2.5%)
Low-Mid	W (1.75%)	W+O+G (12.25%)	W+O+G/O+G (3.5%)	O+G (14%)
Mid-High	W/G (0.5%)	W+O+G/G (2.5%)	W+O+G/O+G/G (1.333%)	O+G/G (5%)
High	G (2%)	G (14%)	G (8%)	G (16%)

TABLE III
PARAMETERS FOR THE OUTPUT MEMBERSHIP FUNCTIONS BASED ON THE
OUTPUT OF THE INFERENCE ENGINE.

	gas+oil		oil+water
gas	0 (a), 0.5 (b), 1 (c)	oil	0 (a), 0.5 (b), (c)1
gas-oil	0.5 (a), 1, 1.5 (c)	oil-water	0.5 (a), 1 (b), 1.5 (c)
oil	1 (a), 1.5 (b), 2 (c)	water	1 (a), 1.5 (b), 2 (c)

are evaluated with given input, and thus all consequences are inferred, the results, i.e. fuzzy subsets, are aggregated as one fuzzy set for defuzzification.

3) Defuzzification: Defuzzification is to convert the aggregated result to a crisp value. the *center of gravity (COG)* determination is utilised here to defuzzify the input fuzzy set from inference engine. *COG* is defined as:

$$q^* = \begin{cases} -1 & \int \mu_{F_o}(q)\mathrm{d}q = 0 \\ \frac{\int q\mu_{F_o}(q)\mathrm{d}q}{\int \mu_{F_o}(q)\mathrm{d}q} & otherwise \end{cases} \quad (16)$$

where q^* is the output value, F_o is the aggregated fuzzy set, $\mu_{F_o}(q)$ is the aggregated output MF, and q is the output variable of the output MF. Further with the previous example, the defuzzified values using COG are -1 and 1 for *gas+oil* and *oil+water*, respectively.

C. Image post-processing

The post-processing is to decompose mixture to individual phase and its ratio. The output from the FIS contains two important information: one is the possible combination of gas, oil, and/or water, and the other is the degree of each component, i.e. the concentration of each phase. Let $D_x = \{d_i^x | i \in \{1, 2, \cdots\}\}$ represent defuzzified values, where x is either $gas + oil$ or $oil + water$, and $d_i^x \in \{-1\} \cup [0, 2]$. According to the definition of the output MF (Fig. 6) and COG defuzzification definition (16), d_i^x can be categorised into 4 sub-spaces, within which the mixture contains different components:

$$mixture_{p,q} = \begin{cases} N/A & d_i^x = -1 \\ p & d_i^x \in [0, 0.5] \\ p+q & d_i^x \in (0.5, 1.5) \\ q & d_i^x \in [1.5, 2] \end{cases} \quad (17)$$

where p and q are gas and oil for $gas + oil$ output, or oil and water for $oil + water$, and N/A means the $mixture_{p,q}$ contributes nothing to final result. By combining both $mixture_{gas,oil}$ and $mixture_{oil,water}$, a decision tree can be built up to determine possible phases and their ratios, i.e. local concentration of each phase. The decision tree is
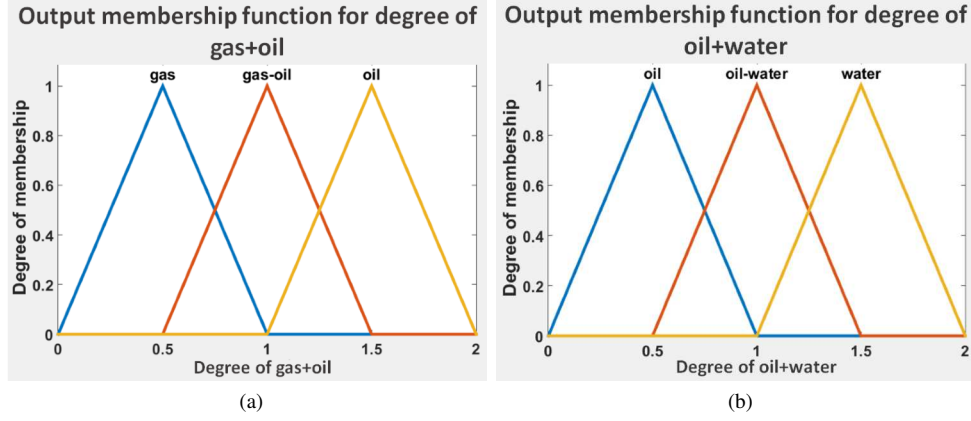
Fig. 6. The output membership functions for the degree of (a) gas+oil and (b) oil+water from the inference engine.
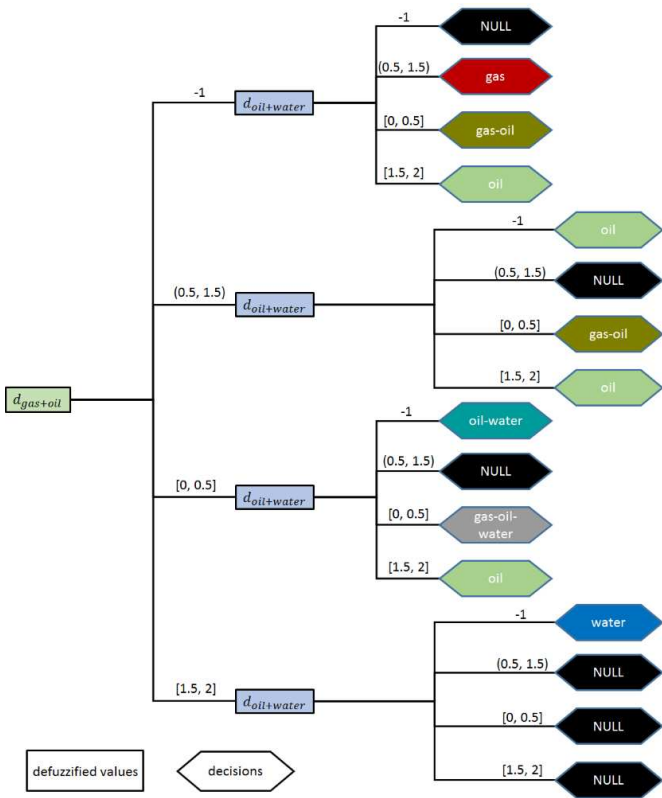

Fig. 7. Decision tree for determining possible phases with given defuzzified values.

depicted in Fig. 7, in which *NULL* means negative decisions, i.e. impossible combinations by given conditions. Furthermore, local concentrations for the decision nodes can be calculated. When the result is single phase, the concentration is 1 for that phase. The concentrations for the phases, i.e. gas-oil, oil-water, and gas-oil-water, can be calculated by (18), (19), and (20), respectively.

$$
\alpha_i = \begin{cases} \alpha_g & = (d_i^{gas+oil} - 0.5) * 100 \\ \alpha_o & = (1.5 * 100 - \alpha_{gas}) = (1.5 - d_i^{gas+oil}) * 100 \\ \alpha_w & = 0 \end{cases} \tag{18}
$$

$$
\alpha_i = \begin{cases} \alpha_g & = 0 \\ \alpha_o & = (d_i^{oil+water} - 0.5) * 100 \\ \alpha_w & = 1 * 100 - \alpha_o = (1.5 - d_i^{oil+water}) * 100 \end{cases} \tag{19}
$$

$$
\alpha_i = \begin{cases} \alpha_g & = (d_i^{gas+oil} - 0.5) * 100 \\ \alpha_o & = (1 * 100 - \alpha_g) \times (d_i^{oil+water} - 0.5) \\ \alpha_w & = 1 * 100 - \alpha_g - \alpha_o \end{cases} \tag{20}
$$

where α_g, α_o, and α_w are local concentrations at i for gas, oil, and water, respectively. After the mixture has been decomposed and the concentration of each phase has been computed, the image is going to be displayed using colour mapping.

After the decomposition, the local concentrations for all phases need to be mapped to RGB colours. Let $P = \{p_i | i \in \{1, 2, \cdots, X \times Y\}]\}$ denote concentration space for an image with resolution $X \times Y$. Every p_i comprises three components, i.e. α_i^g, α_i^o, and α_i^w, of which the relationship between them is governed by:

$$
p_i = (\alpha_i^g, \alpha_i^o, \alpha_i^w); \ \alpha_i^g + \alpha_i^o + \alpha_i^w = 100\%, \alpha_i^x \in [0, 100\%] \tag{21}
$$

where x is g, o, and w. Let $RGB = \{c_i | i \in \{1, 2, \cdots\}\}$ denote a RGB colour space, of which every c_i is composed of three components, i.e. red, green, and blue, which satisfies:

$$
c_i = (r, g, b); \ r, g, and \ b \in [0, 255] \tag{22}
$$

Based on (21) and (22), a simple mapping function can be applied using matrix multiplication:

$$
\begin{bmatrix} r_i & g_i & b_i \end{bmatrix} = \begin{bmatrix} \frac{\alpha_i^g}{100} & \frac{\alpha_i^o}{100} & \frac{\alpha_i^w}{100} \end{bmatrix} \begin{bmatrix} 255 & 0 & 0 \\ 0 & 255 & 0 \\ 0 & 0 & 255 \end{bmatrix} \tag{23}
$$

Since the concentration values are continuously distributed within the range [0,1], colours have to be continuous when mapping the vectors to colours, and thus a triangle RGB colour space has to be considered. In this paper, a triangle RGB colour space similar to the one in [10] is employed for the mapping and displaying, as depicted in Fig. 8.
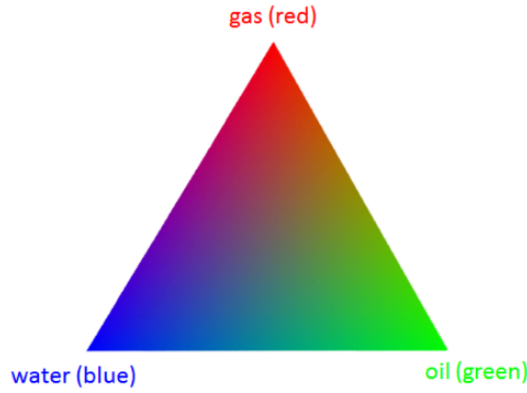
Fig. 8. Triangle RGB colour space.

TABLE IV
PHYSICAL PROPERTIES OF EACH PHASE.

	Gas	Oil	Water
Fluid	Nitrogen	Paraflex	Salty water
Conductivity (mS/cm)	0	0	33.5
Dielectric constant (ε)	1	2.2	80
Dynamic viscosity (cP)	0.0174	16.18	1.35
Density (kg/m^3)	12	830	1049.1

TABLE V
SELECTED FLOW CONDITIONS FOR EVALUATING THE PROPOSED
APPROACH.

	WLR (%)	GVF (%)
Stratified flow	50	60
Wavy stratified flow	75	40
Slug flow	75	42
Plug flow	75	5
Annular flow	90	92
Bubbly flow	90	35

IV. EVALUATION

Experiments were carried out on gas-oil-water flow in industry-scale flow facilities in TUV NEL UK[1]. In the experiments, nitrogen was utilized as gas phase, Paraflex (HT9) was as oil phase, and salty water was as water phase, with pressure at 10 bars and temperature at 20 degree. The physical properties of each phase is listed in Table IV. Different Water-in-Liquid Ratio (WLR) and Gas Volume Fraction (GVF) were combined in order to produce common flow regimes in horizontal pipe. The selected testing matrix for the evaluation of the proposed imaging approach is shown as Table V.

The position and the structure of the deployed sensors of ERT and ECT are depicted in Fig. 9. The ERT system employs 2 rings of 16 evenly-mounted electrodes, and the ECT system employs 12 electrodes. Since they are two standalone systems, they are positioned along the pipe at different points. It is worth noting that to avoid the interference between each other, they are separated for a short distance which is ignored in the data processing. In order to measure fully developed flow, the
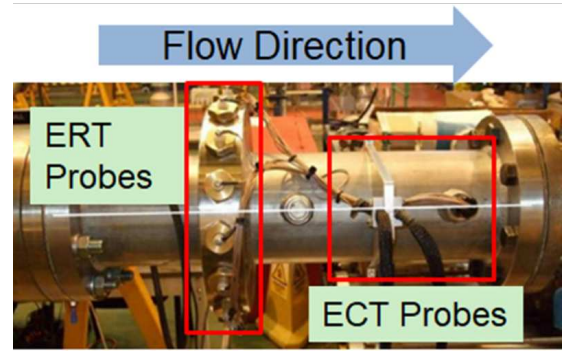
Fig. 9. The position and structure of the ERT/ECT sensors for the experiment.

sensors are located over 150D away from the injection point, where D is the diameter of the pipe. During the experiment, the systems were manually synchronised by two operators.

The evaluation is separated into two parts: one is to appraise the feasibility of the proposed approach for different flow regimes with the same membership functions; and the other is to check the robustness with different definitions of input MFs using one flow regime.

It should be pointed out that the measured mean concentrations are from local tomograms. Due to the lack of the local information, e.g. phase velocity and local pressure at the sensing location, the local concentrations are unable to be derived. The only available reference information is the reference volume fraction based on the volumetric flowrate at feed-in point. Although it is not the most appropriate one, the comparison between the measured mean concentrations and the volume fractions from WLR and GVF would still provide useful information due to their obvious correlation. To avoid potential confusion, hereafter, the terms of void fraction and volume fraction are used to correspond the local mean concentration at sensing location and reference volume fraction at feed-in point, respectively. In addition, for the convenience of the comparison, the reference volume fractions are presented in percentage.

A. Feasibility

The results are depicted in Fig. 10. For each flow regime, stacked images from high-speed camera and three axial cross-sectional images extracted from 500 consecutive frames are displayed by ECT, ERT, and fuzzy logic-based fusion. From visual perspectives, the proposed approach, overall, is able to produce fused images competitive with the ones by the reference. When ECT and ERT are able to identify, although approximately, the interface between each phase, e.g. in Fig. 10b, FIS-based approach generates qualitative images very close to the reference ones, despite some distortion close to the interface. This, however, reflects the limitations of electrical tomographic system, e.g. blurred boundaries between gas and liquid. However, FIS-based fused images is incapable of presenting good-quality tomograms for the annular flow (Fig. 10e) and the bubbly flow (Fig. 10f). For bubbly flow, the bubbles are too small to be visualised by both ERT and ECT, thereby the tomograms being distorted (Fig. 10f). For

TABLE VI
MEAN CONCENTRATIONS OF DIFFERENT FLOW REGIMES BY THE REFERENCE AND THE PROPOSED APPROACH.

		gas (%)	oil (%)	water (%)
Stratified flow	Reference (volume fraction)	60	20	20
	FIS (void fraction)	48.15	21.08	30.77
wavy Stratified flow	Reference (volume fraction)	40	15	45
	FIS (void fraction)	51.84	14.18	33.97
Slug flow	Reference (volume fraction)	42	14.5	43.5
	FIS (void fraction)	47.58	17.5	34.92
Plug flow	Reference (volume fraction)	5	23.75	71.25
	FIS (void fraction)	5.92	58.38	35.58
Annular flow	Reference (volume fraction)	92	0.8	7.2
	FIS (void fraction)	93.72	4.06	2.22
Bubbly flow	Reference (volume fraction)	35	6.5	58.5
	FIS (void fraction)	0.97	74.27	24.76

annular flow, when the liquid film is too thin, both modalities are unable to identify it, e.g. the film on the top. In contrast, ECT manages to visualise the bottom film (the bottom part in the second image of Fig. 10e), whereas the ERT tomograms (the third image in Fig. 10e) present some distortion. This is probably because oil in the liquid mixture affects the measurement of ERT. Table VI lists the mean concentrations for all tested flow conditions by the proposed approach, which reveals similar situations to those by the observation.

B. Robustness

In the robustness evaluation, four different input MFs are examined as listed in Table VII. The selected flow regimes is stratified flow. The first set of experiments is conducted by fixing the ECT MFs but changing the ERT MFs, and the second set of experiments is conducted by fixing the ERT MFs but changing the ECT MFs. The fused imaged are depicted in Fig. 11 and the mean concentrations from different MFs are listed in Table VIII.

From qualification point of view, all images from both sets are hardly distinguishable in visual terms. The similarity of the images demonstrates that the MF changes have little impact on the visualisation, which further proofs the robustness of the proposed method. From a quantification perspective, the noticeable changes of the ERT MFs result in the trivial fluctuations of phase concentrations (the upper part of Table VIII). When it comes to the different ECT MFs, the outcome (the lower part of Table VIII) is similar, although the gas concentration changes from 46.62% to 50.08%. This is primarily because the blurry boundaries between gas and liquid in the ECT tomograms. Nevertheless, despite of the significant changes of the ECT MFs, the quantitative results evidence that the FIS is, in essence, insensitive to MF changes.

V. CONCLUSIONS

A novel approach has been proposed to resolve the problems associated with multi-dimensional data fusion by multi-modality electrical tomographic system for visualisation and measurement of gas-oil-water flow in industrial sectors.

Through the approach, images from different electrical tomographic systems are integrated along spatial and temporal dimensions, and hence gas-oil-water flow is visualised with certain information about multiphase flow dynamics. A key advantage of the proposed approach over the conventional threshold-based methods is that it does not require a *priori* knowledge to pinpoint threshold values for the fusion. A direct consequence of the advantage is that the proposal is insensitive to the changes of different membership functions, resulting in robust outcomes in both qualitative and quantitative terms. With the assistance of the decision tree, the approach is also able to present quantitative results, i.e. concentration distributions of the individual phases in the flow, which are substantially important in multiphase flow characterisation.

Since the input into the proposed approach is the concentration distribution of the phases involved in the flow, rather than reconstructed conductivity or permittivity variation, this could extend the suitability of the approach for other modalities, e.g. displacement-current phase tomography (DCPT) and ECT [29], with little modification, since the concentration tomograms required by the approach could be derived from the conductivity distribution by DCPT as well. More generally, the approach may be extended to be applicable to the modalities producing concentration distributions of different phases in gas-oil-water three-phase flow, e.g. one derives the water concentration and the other derives the oil concentration. But in this case, the possible phase combinations (i.e. Fig. 4) may need to be updated according to the actual meanings of the input concentration distributions.

In spite of its feasibility and robustness in the domain of multiphase flow imaging, there are a few aspects need to be addressed in the future. One suspicious error source in the approach is introduced by the spatial and temporal registration of the images because two modalities deployed are standalone. The error could be diminished by the integration of both modalities, e.g. the ones described in [14] and [16]. Another aspect is the application of different membership functions. Although the ones applied in this study proved to be better than others [28] in some other applications, it is still unclear whether they yield the same advantages in multiphase flow-involved image fusion. Higher-resolution
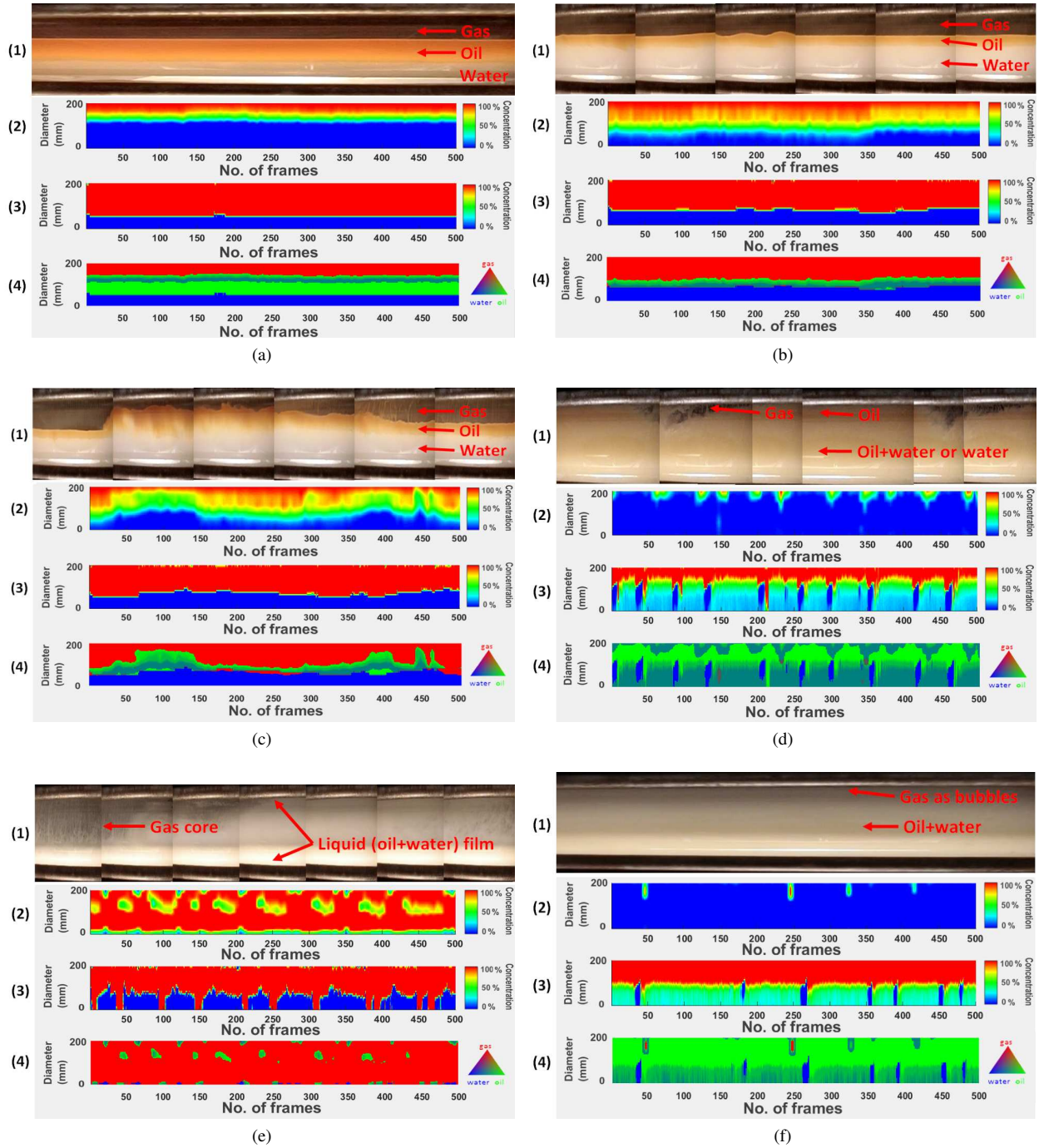
Fig. 10. Images by high-speed video and axial stacked concentration images for stratified flow by ECT (1), ERT (2), and fuzzy logic-based fusion (the fourth), for (a) stratified flow; (b) wavy stratified flow; (c) slug flow; (d) plug flow; (e) annular flow; and (f) bubbly flow.

TABLE VII
DIFFERENT INPUT MF DEFINITIONS BASED ON VOID FRACTION.

	low-mid input MF	mid-high input MF	high input MF
Case 1	0.05 (a), 0.225 (b), 0.4 (c)	0.25 (a), 0.4 (b), 0.55 (c)	0.4 (x), 0.5 (y), 1.033 (z), 1.3 (w)
Case 2	0.05 (a), 0.25 (b), 0.45 (c)	0.3 (a), 0.45 (b), 0.6 (c)	0.45 (x), 0.55 (y), 1.033 (z) 1.3 (w)
Case 3	0.05 (a), 0.275 (b), 0.5 (c)	0.35 (a), 0.5 (b), 0.65 (c)	0.5 (x), 0.6 (y), 1.033 (z) 1.3 (w)
Case 4	0.05 (a), 0.3 (b), 0.55 (c)	0.4 (a), 0.55 (b), 0.7 (c)	0.55 (x), 0.65 (y), 1.033 (z) 1.3 (w)

images by advanced reconstruction algorithms, e.g. SCG [30]   or others in [31] should be incorporated to make improvements
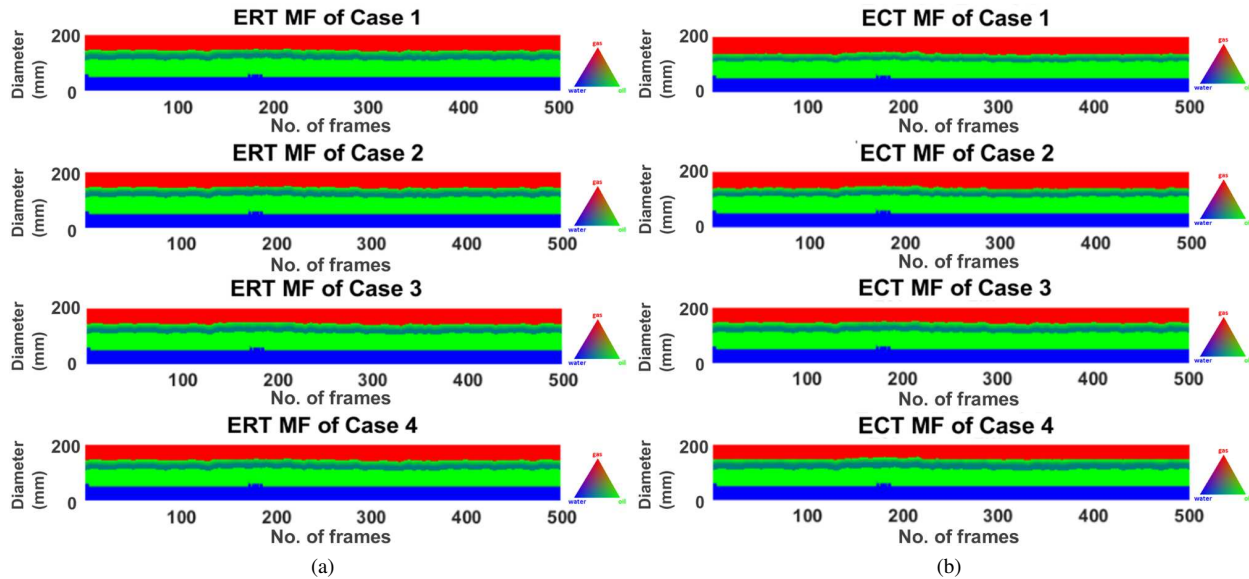
Fig. 11. FIS-fused images for the stratified flow by (a) different MFs for ERT but the same ECT MF, and (b) different MFs for ECT but the same ERT MF.

TABLE VIII
MEAN CONCENTRATIONS OF THE FLOW PHASES WITH DIFFERENT MFs DEFINED IN TABLE VII.

	α_{gas} (%)	α_{oil} (%)	α_{water} (%)
Case 1 (ERT MFs)	48.15	21.27	30.58
Case 2 (ERT MFs)	48.15	21.16	30.69
Case 3 (ERT MFs)	48.14	21.08	30.78
Case 4 (ERT MFs)	47.98	20.87	31.15
Case 1 (ECT MFs)	50.08	19.15	30.77
Case 2 (ECT MFs)	49.20	20.03	30.77
Case 3 (ECT MFs)	48.14	21.08	30.77
Case 4 (ECT MFs)	46.62	22.61	30.77

to the outcomes, and meanwhile address the possible error sources in the process.

REFERENCES

[1] U. E. I. Administration, "Annual energy outlook," Website, 2016, accessed on June 2016. [Online]. Available: https://www.eia.gov/analysis/
[2] R. Thorn, G. A. Johansen, and B. T. Hjertaker, "Three-phase flow measurement in the petroleum industry," *Measurement Science and Technology*, vol. 24, no. 1, p. 012003, 2013.
[3] M. Wang, Ed., *Industrial Tomography Systems and Applications*. Woodhead Publishing, 2015.
[4] B. S. Hoyle, F. J. W. Podd, H. I. Schlaberg, M. Wang, R. A. Williams, and T. A. York, "Multi-sensor process tomography system design: Part 1–systems and hardware engineering," in *1st World Congress on Industrial Process Tomography*, 1999, pp. 323–327.
[5] A. P. James and B. V. Dasarathy, "Medical image fusion: A survey of the state of the art," *Information Fusion*, vol. 19, pp. 4 – 19, 2014, special Issue on Information Fusion in Medical Image Computing and Systems.
[6] R. S. Blum and Z. Liu, *Multi-sensor image fusion and its applications*. CRC press, 2005.
[7] B. S. Hoyle and M. Wang, "Multi-dimensional opportunities and data fusion in industrial process tomography," in *Instrumentation and Measurement Technology Conference (I2MTC), 2012 IEEE International*, May 2012, pp. 916–920.
[8] B. Hoyle, X. Jia, F. Podd, H. Schlaberg, H. Tan, M. Wang, R. W. R.M. West, and T. York, "Design and application of a multi-modal process tomography system," *Measurement Science and Technology*, vol. 12, no. 8, p. 1157, 2001.
[9] B. Hjertaker, R. Maad, and G. A. Johansen, "Dual-mode capacitance and gamma-ray tomography using the landweber reconstruction algorithm," *Measurement Science and Technology*, vol. 22, no. 10, p. 104002, 2011.
[10] E. N. dos Santos, T. P. Vendruscolo, R. E. M. Morales, E. Schleicher, U. Hampel, and M. J. D. Silva, "Dual-modality wire-mesh sensor for the visualization of three-phase flows," *Measurement Science and Technology*, vol. 26, no. 10, p. 105302, 2015.
[11] M. Wang, F. J. Dickin, and R. Mann, "Electrical resistance tomography sensing systems for industrial applications," *Chemical Engineering Communications*, vol. 175, no. 1, pp. 49–70, 1999.
[12] W. Q. Yang and L. Peng, "Image reconstruction algorithms for electrical capacitance tomography," *Measurement Science and Technology*, vol. 14, no. 1, p. R1, 2003.
[13] C. Qiu, B. Hoyle, and F. Podd, "Engineering and application of a dual-modality process tomography system," *Flow Measurement and Instrumentation*, vol. 18, no. 5-6, pp. 247 – 254, 2007, process Tomography and Flow Visualization.
[14] Q. Marashdeh, W. Warsito, L. Fan, and F. L. Teixeira, "A multimodal tomography system based on ect sensors," *IEEE Sensors Journal*, vol. 7, no. 3, pp. 426–433, March 2007.
[15] J. Sun and W. Yang, "A dual-modality electrical tomography sensor for measurement of gasoilwater stratified flows," *Measurement*, vol. 66, pp. 150 – 160, 2015.
[16] H. Ji, W. Tan, Z. Gui, B. Wang, Z. Huang, H. Li, and G. Wu, "A new dual-modality ect/ert technique based on c4d principle," *IEEE Transactions on Instrumentation and Measurement*, vol. 65, no. 5, pp. 1042–1050, 05 2016.

[17] B. Hjertaker, R. Maad, and G. A. Johansen, "Dual-mode capacitance and gamma-ray tomography using the landweber reconstruction algorithm," *Measurement Science and Technology*, vol. 22, no. 10, p. 104002, 2011.

[18] F. Fischer and U. Hampel, "Ultra fast electron beam x-ray computed tomography for two-phase flow measurement," *Nuclear Engineering and Design*, vol. 240, no. 9, pp. 2254 – 2259, 2010, experiments and {CFD} Code Applications to Nuclear Reactor Safety (XCFD4NRS).

[19] Q. Wang, M. Wang, K. Wei, and C. Qiu, "Visualization of gas-oil-water flow in horizontal pipeline using dual-modality electrical tomographic systems," *IEEE Sensors Journal*, vol. 17, no. 24, pp. 8146–8156, Dec 2017.

[20] S. Yue, T. Wu, J. Pan, and H. Wang, "Fuzzy clustering based et image fusion," *Inf. Fusion*, vol. 14, no. 4, pp. 487–497, Oct. 2013.

[21] J. Pusppanathan, M. Faramarzi, F. R. Yunus, N. M. N. Ayob, R. A. Rahim, F. A. Phang, M. H. F. Rahiman, A. Ahmad, L. P. Ling, and K. H. Abas, "Image fusion using fuzzy logic pixel fusion for dual modality tomography system," *Jurnal Teknologi*, vol. 70, no. 3, 2014.

[22] Q. Wang and M. Wang, "Thresholding values and fuzzy logic fusion in visualisation of gas-oil-water horizontal flow using dual-modality electrical tomography," in *Proceedings of 9th World Congress on Industrial Process Tomography*, vol. 9. International Society for Industrial Process Tomography (ISIPT), 2019, pp. 749–758.

[23] M. Wang, Q. Wang, and B. Karki, "Arts of electrical impedance tomographic sensing," *Philosophical Transactions of the Royal Society A*, 2016.

[24] J. Jia, M. Wang, and Y. Faraj, "Evaluation of eit systems and algorithms for handling full void fraction range in two-phase flow measurement," *Measurement Science and Technology*, vol. 26, no. 1, p. 015305, 2015.

[25] F. Capolino, *Theory and Phenomena of Metamaterials*, first edition ed. CRC Press, 2009, vol. 1.

[26] ITS, *ITS System 2000 Version 7.0 p2+ Electrical Resistance Tomography System - Users Manual*, Industrial Tomography Systems Plc., Speakers House, 39 Deansgate, Manchester M3 2BA, Nov. 2009.

[27] H.-J. Zimmermann, "Fuzzy set theory," *Wiley Interdisciplinary Reviews: Computational Statistics*, vol. 2, no. 3, pp. 317–332, 2010.

[28] J. Zhao and B. K. Bose, "Evaluation of membership functions for fuzzy logic controlled induction motor drive," in *IECON 02 [Industrial Electronics Society, IEEE 2002 28th Annual Conference of the]*, vol. 1, Nov 2002, pp. 229–234 vol.1.

[29] C. Gunes, Q. M. Marashdeh, and F. L. Teixeira, "A comparison between electrical capacitance tomography and displacement-current phase tomography," *IEEE Sensors Journal*, vol. 17, no. 24, pp. 8037–8046, Dec 2017.

[30] M. Wang, "Inverse solutions for electrical impedance tomography based on conjugate gradients methods," *Measurement Science and Technology*, vol. 13, no. 1, p. 101, 2002.

[31] K. Wei, C. Qiu, M. Soleimani, and K. Primrose, "ITS reconstruction tool-suite: An inverse algorithm package for industrial process tomography," *Flow Measurement and Instrumentation*, vol. 46, Part B, pp. 292 – 302, 2015, special issue on Tomography Measurement & Modeling of Multiphase Flows.